

# Chapter 11

## A Basic Introduction to Quantum Noise and Quantum-Non-Demolition Techniques

Stefan Hild

**Abstract** For the past 120 years the Michelson interferometer has served as the standard tool for high precision length measurements. Starting from the very first Michelson interferometer to today's large-scale gravitational wave observatories, the peak sensitivity of the Michelson interferometer has improved by about 10 orders of magnitude. Advanced gravitational wave detectors, such as Advanced LIGO or Advanced Virgo, will achieve a measurement precision limited by the Heisenberg Uncertainty Principle, giving rise to the interferometric Standard Quantum Limit for 40 kg test masses. This chapter will give a basic outline of the concepts currently under consideration for surpassing the Standard Quantum Limit.

### 11.1 How to Approach This Chapter

In this chapter we will discuss the notion of *quantum noise* and some methods by which it can be reduced in laser-interferometric Gravitational Wave (GW) detectors<sup>1</sup>. It needs to be pointed out that a comprehensive discussion of this topic is far beyond what is possible within the limited space here. So, the reader might wonder what can be gained from reading this chapter? In this chapter I will give my best, trying to approach quantum noise and quantum-non-demolition (QND) techniques from the standpoint of an experimental physicist who aims at thinking in terms of clear and lightweight models with easy applicability, rather avoiding excessive theoretical formalism; hence, my main goal is to convey an intuitive understanding of the underlying concepts of quantum noise and interferometry techniques aiming to

---

<sup>1</sup> Please note, that if not stated explicitly otherwise, we neglect in this chapter all other fundamental noises, such as thermal noise, as well as the myriad of technical noises that commissions of GW detectors have to battle with.

---

S. Hild (✉)

SUPA, Institute for Gravitational Research, University of Glasgow, Glasgow G12 8QQ, UK  
e-mail: stefan.hild@ligo.org

reduce this noise. While this approach requires certain simplifications to be made, the presented formalism will help to foster a qualitative understanding of the underlying phenomena and may serve as a springboard for an in-depth study of the topic.

If you are looking for a mathematically exact description of quantum noise and QND techniques, please stop reading here and please be deferred to one of the excellent books and articles already existing [1–4]. Otherwise, please lean back and enjoy the beauty of interferometry experiments at and beyond the quantum limit!

## 11.2 The Basics of Quantum Noise

The notation *quantum noise* originates from the fact that this noise is a direct consequence of the quantum nature of light. For two reasons quantum noise plays a very special role in the noise-cocktail of advanced laser-interferometric GW detectors:

First of all, quantum noise is of a different nature compared to most other limiting noise sources, because quantum noise originates directly from measurement and readout processes (in contrast to, for example, seismic excitation or thermally driven fluctuations which directly change the position of test mass surfaces). Secondly, as can be seen in Fig. 11.1, quantum noise is the noise source directly limiting the sensitivity of advanced GW detectors over most frequencies of the detection band.

Hence, reducing the quantum noise contribution by means of clever interferometry concepts is of the highest priority if we want to further improve the sensitivity of future GW detectors. So, let us start our quest!

### 11.2.1 Principles for Building a GW Detector

Before we have a closer look at the nature of quantum noise and what processes lead to its presence in the GW channel of the interferometer, it is helpful to recall what is required for conceiving a GW detector with good performance. Although the current laser-interferometric GW detectors are extremely complex machines, a successful design can be boiled down to two basic design principles:

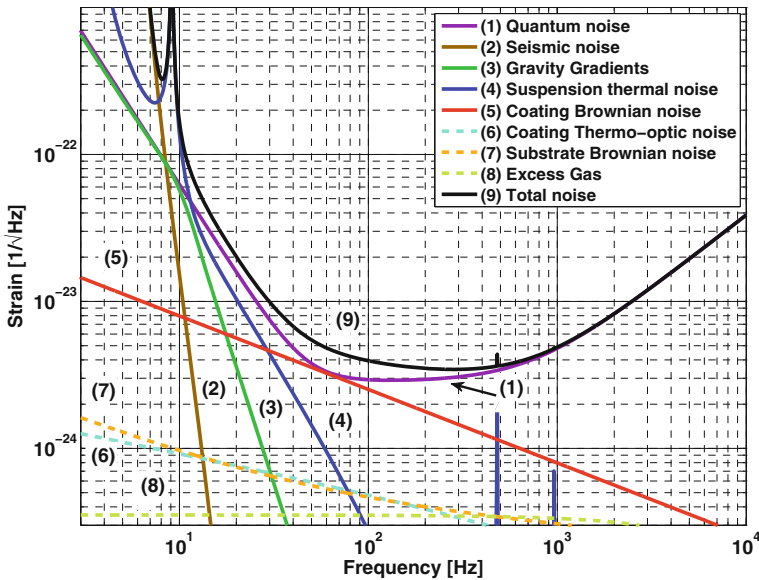


**Fig. 11.1** Noise budget of the advanced LIGO broadband configuration as described in Abbott et al. [5]. The *coloured lines (1–8)* represent the amplitude spectral density of various noise components, whereas the trace labelled “Total Noise” shows the overall instrument sensitivity. For all frequencies above about 12 Hz quantum noise is the dominating noise source (This figure was produced using the GWINC software [6])

1. You need to make sure your test masses are quieter than the signal you want to observe.
2. You need to make sure that the test mass position can be read out to the required accuracy, without introducing any significant level of back action noise.

In order to satisfy the first of the requirements stated above we employ a myriad of sophisticated techniques and we exercise the greatest care when it comes to providing seismic isolation of the test masses, put them into ultra-high vacuum to reduce their acoustic coupling, and use ultra-low loss materials for the test masses as well as for their suspensions to reduce the influence of thermal noise. The second design principle relates fundamentally the optical readout and the interferometric measurement of the differential arm length degree of freedom of the GW detector.

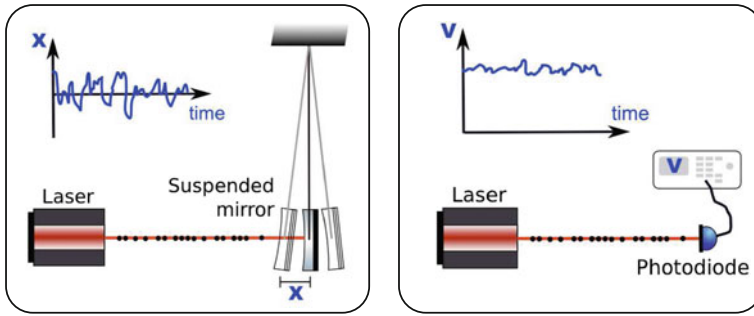


**Fig. 11.2** Illustrations of radiation pressure noise (*left*) and shot noise (*right*)

### 11.2.2 Photon Shot Noise and Quantum Radiation Pressure Noise

So, finally let us answer the question of what quantum noise is actually composed of. It is ultimately made up from two components: photon shot noise at high frequencies and photon radiation pressure noise at the low frequency end of the detection band. The most straightforward way to understand the origin of the two quantum noise components is illustrated in Fig. 11.2. The photons in a laser beam are not equally spaced in time, but follow a Poissonian distribution. Consequently, when a laser is shone onto a photodetector, the resulting time-series of the photo current is not constant over time but is subject to fluctuations. These fluctuations, literally also called shot noise, increase proportional to the *square root* of the optical power in the laser beam. In contrast, the signal strength in the GW detector increases *linearly* with the optical power. Hence, by increasing the optical power in a GW detector the signal-to-shot-noise ratio can be effectively increased, proportional to the square root of the optical power inside the GW interferometer. The amplitude spectral density of strain equivalent of photon shot noise in a simple Michelson interferometer (without arm cavities or recycling) can be expressed as

$$h_{\text{sn}}(f) = \frac{1}{L} \sqrt{\frac{\hbar c \lambda}{2\pi P}}, \quad (11.1)$$

where  $f$  is the frequency,  $L$  is the arm length of the GW detector,  $c$  is the speed of light,  $\lambda$  the laser wavelength, and  $P$  the optical power in the interferometer arms.

The second effect of the temporally inhomogeneous distribution of the photons in a laser beam is illustrated on the left panel of Fig. 11.2. Photons carry momentum and when they are reflected from a free-falling test mass they transfer momentum, or better, a radiation pressure force onto the mirror. Since the photons do not arrive at the test mass with exactly similar separation in time, the force onto the mirror and therefore also its position fluctuate over time, giving rise to photon radiation pressure noise. The amplitude spectral density of the quantum radiation pressure noise in a simple Michelson is given by

$$h_{\text{rp}}(f) = \frac{1}{mf^2L} \sqrt{\frac{\hbar P}{2\pi^3 c\lambda}}, \quad (11.2)$$

where  $m$  is the mass of the mirror. In contrast to shot noise we see that the radiation pressure noise spectrum is not white, but its contribution falls off as  $1/f^2$ . From this it is obvious that radiation pressure noise will dominate at low frequencies, while shot noise is the dominant contribution at high frequencies.

We define the quantum noise of an interferometer to be the (uncorrelated) sum of photon shot noise and photon radiation pressure noise.

### 11.2.3 The Standard Quantum Limit

It is important to note in Eqs. 11.1 and 11.2 that shot noise and radiation pressure noise scale inversely with the optical power inside the Michelson interferometer; so, while it is possible to improve the strain sensitivity of an interferometer at high frequencies by increasing the circulating light power, inevitably at the same time the sensitivity will decrease at low frequencies as the radiation pressure increases with the light power. This relation is illustrated in Fig. 11.3. Ultimately, for every observation frequency there exists an optimal power, which results in identical magnitude contributions from shot noise and quantum radiation pressure noise at this frequency. For example, the best sensitivity at a frequency of 8 Hz is achieved for 1 MW (see trace 2c in Fig. 11.3). The Standard Quantum Limit (SQL) is defined as the lower bound envelope of the quantum noise spectra for all optical powers circulating in interferometer with a specific set of design parameters [7]. As illustrated in Fig. 11.3, the SQL for a simple Michelson interferometer follows a slope inverse to the observation frequency.

The SQL has originally been suggested as an ultimate limit for the sensitivity of laser interferometers that cannot be surpassed. However, it was quickly realized that the SQL only imposes a limit on the achievable sensitivity of classical interferometers but that there are several techniques, such as detuned signal recycling and quantum non-demolition configurations, which can enable interferometric measurements with displacement sensitivities below the SQL. The basic principles of the most prominent techniques that allow us to beat the SQL will be discussed in the following sections.

## 11.3 A Simple Graphical Tool to Understand Quantum Noise

### 11.3.1 The Quadrature Picture

In order to gain an intuitive understanding of quantum noise in interferometric measurements, in the following we will introduce a rather simple, yet powerful graphical

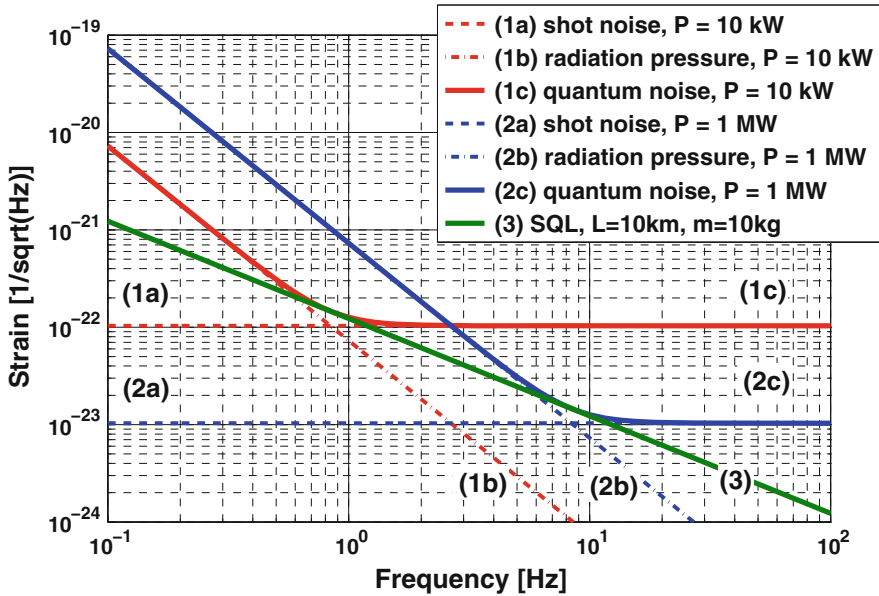


**Fig. 11.3** The SQL (trace 3) and the quantum noise contribution for a simple Michelson interferometer, featuring 10 km arm length and test masses of 10 kg weight, for low (traces 1a–1c) and high (traces 2a–2c) circulating power

tool, often formally referred to as the *quadrature picture* or informally sometimes referred to as the *ball on a stick picture*.

In general we can describe an electric field  $\mathbf{E}$  at a position  $\mathbf{r}$  and at the time  $t$  by

$$\mathbf{E}(\mathbf{r}, t) = E_0 \left[ a(\mathbf{r})e^{-i\omega t} - a^*(\mathbf{r})e^{+i\omega t} \right] \mathbf{p}(\mathbf{r}, t), \tag{11.3}$$

where  $a$  is the complex amplitude of the electro-magnetic field,  $\omega$  its angular frequency and  $\mathbf{p}$  the polarization. We can introduce the following two new properties:

$$X_1(\mathbf{r}) = a^*(\mathbf{r}) + a(\mathbf{r}) \tag{11.4}$$

$$X_2(\mathbf{r}) = i \left[ a^*(\mathbf{r}) - a(\mathbf{r}) \right]. \tag{11.5}$$

$X_1$  and  $X_2$  are usually referred to as the amplitude and phase quadrature, respectively. Using the quadrature representation we can now rewrite Eq. 11.3 to express the electromagnetic field in terms of the amplitude and phase quadratures:

$$\mathbf{E}(\mathbf{r}, t) = E_0 \left[ X_1 \cos(\omega t) - X_2 \sin(\omega t) \right] \mathbf{p}(\mathbf{r}, t). \tag{11.6}$$

In close analogy to Eqs. 11.4 and 11.5 we can formulate the so-called quadrature operators which are the foundation of a description of light fields in the realm of quantum mechanics as

$$\hat{X}_1(\mathbf{r}) = \hat{a}^\dagger(\mathbf{r}) + \hat{a}(\mathbf{r}) \quad (11.7)$$

$$\hat{X}_2(\mathbf{r}) = i \left[ \hat{a}^\dagger(\mathbf{r}) - \hat{a}(\mathbf{r}) \right], \quad (11.8)$$

where  $\hat{X}_1(\mathbf{r})$  is the **amplitude quadrature operator** and  $\hat{X}_2(\mathbf{r})$  is the **phase quadrature operator**.

### 11.3.2 The Ball on a Stick Picture

A common way to visualize the quadrature operators introduced above is the “ball on the stick” picture. In the following we use a concept similar to that which has been introduced for example by Chen [8, 9]. The left-hand side of Fig. 11.4 shows an example of a coherent light field. Let us assume the light field consists of a huge number of photons and we continuously perform measurements over a finite duration to determine the *light states*. We can represent each measurement by a single dot in the  $\hat{X}_1, \hat{X}_2$  plane. If we perform a large number of measurements, then we can measure the probability distribution of the light state, which is indicated by the “ball” or “cloud” shown in Fig. 11.4. The solid arrow points at the center of that ball which is the point in the  $\hat{X}_1, \hat{X}_2$  plane featuring the highest probability to encounter the field in this state if a measurement is carried out. So we can graphically represent the coherent part of a light field (with a certain amplitude and phase) by the arrow shown, while the uncertainty (or noise) of the field is represented by the ball; hence the phrase *ball on a stick*. The quantum nature of light forbids us to reduce the area of the ball below a certain limit, in the following referred to as the uncertainty limit. This limit can be considered to be a direct consequence of the *Heisenberg Uncertainty Principle* which also applies in a quantum-mechanical description of light.

While the uncertainty principle dictates the minimal area of the ball, we have the freedom to manipulate its shape. One way to change the shape of the ball is a technique with the figurative name *squeezing* [10]. The right-hand panel of Fig. 11.4 shows a light field that is squeezed in phase quadrature, i.e., the uncertainty of the light state is reduced in one quadrature (in this case the phase quadrature), while at the same time one has to pay the price of at least a proportionally increased uncertainty in the orthogonal quadrature (in this case the amplitude quadrature). As we will see later in Sects. 11.4 and 11.6, squeezed light can be used to improve the quantum noise limited sensitivity of laser-interferometric gravitational wave detectors.

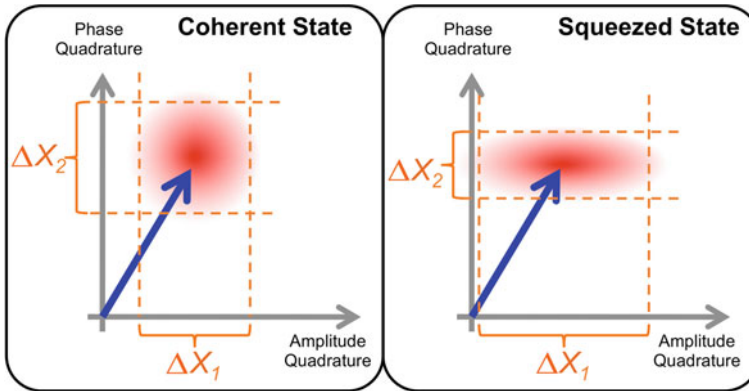


**Fig. 11.4** *Left* Graphical representation of a coherent state in the quadrature picture. Due to the quantum nature of light the photons in a laser beam do not all have the same amplitude and phase, but follow a probability distribution indicated by the ball or cloud. The minimal area of this ball is limited by the uncertainty principle. *Right* Graphical representation of a squeezed state. While the uncertainty in the phase quadrature is reduced, the uncertainty in the amplitude quadrature is increased, so that the ball now takes the shape of an ellipse, i.e., the so-called *squeezing ellipse*

However, for the moment let us go back to the quadrature picture of a conventional, unsqueezed light field and explore how our graphical tool relates to the strain spectrum of quantum noise we previously discussed in Sect. 11.2. The strain spectral density of quantum noise can simply be understood as an inverse signal-to-noise ratio (SNR), or better as a noise-to-signal ratio, where “noise” refers to the amplitude of the quantum fluctuations in the instrument and “signal” refers to the gravitational wave-induced phase change of the light which manifests as the change in the differential arm length scaled with the frequency-dependent signal gain in the instrument. The lower the quantum noise at constant signal amplitude or the higher the signal amplitude at a constant noise level, the lower is the quantum noise limited strain spectral density of the interferometer, i.e., the better is the sensitivity of the instrument.

So, where do we find the quantum noise-limited strain spectral density in our graphical picture? Let us have a look at Fig. 11.5: The second panel shows the uncertainty ball of the light state entering our interferometric system of interest, but in contrast to the previous section we have omitted the filling of the ball and just represent its outline by a circle.<sup>2</sup> In addition, we have drawn two arrows,  $E_1$  and  $E_2$ , representing the noise in the two orthogonal quadratures. Please note that for a coherent state the noise in the two quadratures is completely uncorrelated which is the reason why the two arrows here are displayed in different colors.

When a gravitational wave causes the length of an interferometer arm to change or if a local disturbance moves the position of an interferometer mirror, then this will cause a signal to show up in the phase quadrature, indicated in the third panel

<sup>2</sup> Please note, that the circle does not indicate 100% of the distribution function, but the radius usually corresponds to  $1\sigma$ .



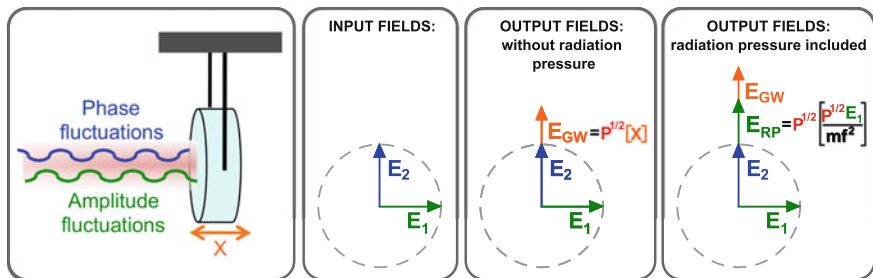


**Fig. 11.5** Illustration of optomechanical coupling of quantum noise on suspended mirrors. The input field is described by the uncorrelated noise contributions  $E_1$  and  $E_2$  in the amplitude and phase quadrature, respectively. Without optomechanical coupling the noise contributions in the phase and amplitude quadrature are uncorrelated. In case the optomechanical coupling becomes dominant, fluctuations in the amplitude quadrature ( $E_1$ ) are converted into fluctuations in the phase quadrature ( $E_{RP}$ ), thereby introducing correlations of the noise components in the two quadratures.  $P$  is the optical power inside the system,  $m$  is the reduced mass of the ensemble of test masses,  $f$  is the frequency, and  $X$  symbolises a test mass displacement or the equivalent strain

of our picture by the short arrow  $E_{GW}$ . To measure our gravitational wave signal we have to decide on a readout angle or quadrature angle. Obviously, in the simple case displayed in the third panel of Fig. 11.5, we obtain the best SNR exactly reading out the phase quadrature; while the magnitude of the noise is similar for all possible readout angles the signal is maximal in the phase quadrature (vertical direction). So let us assume for the moment that, if not stated explicitly otherwise, we always choose a readout angle that perfectly coincides with the phase quadrature.

So far we have not included any optomechanical coupling in our picture, i.e., the situation displayed in the third panel of Fig. 11.5 is only valid for scenarios with negligible radiation pressure (i.e., for high frequencies or very low ratio of optical power and mirror mass). Let us now include the effects of quantum radiation pressure acting on our suspended test masses. As illustrated on the left-hand panel of Fig. 11.5, both phase and amplitude fluctuations are “impinging” onto the test mass. While the phase fluctuations have no mechanical effect on the mirror, the amplitude fluctuations couple via radiation pressure into position fluctuations of the test mass. These position fluctuations then show up, similar to the GW signal, as an additional component in the phase quadrature (see  $E_{RP}$  on the right-hand panel of Fig. 11.5). The key difference between the original fluctuations in the phase quadrature ( $E_2$ ) and the fluctuations optomechanically coupled from the amplitude quadrature into the phase quadrature ( $E_{RP}$ ) is the fact that now we have introduced correlated fluctuations in the amplitude and phase quadrature. As we will see in later sections, these introduced correlations between  $E_1$  and  $E_{RP}$  can be used for beating the SQL. However, for the moment let us get back to the right-hand panel of Fig. 11.5: The magnitude of the radiation pressure induced fluctuations in the phase quadrature, i.e., the length of  $E_{RP}$ , scales directly with the light power, is inverse to the mass of the mirror, and

due to the response function of a suspended mirror to an external force inverse to the frequency squared.

So, now we have completely assembled our graphical tool and it is time to check whether it delivers useful results and predictions. Let us see if we can explain the individual traces in Fig. 11.3. For the low power case (traces 1a–1c) at high frequencies radiation pressure does not play any role and the sensitivity of the interferometer is limited by the ratio of the shot noise in phase quadrature ( $E_2$ ) and the GW signal ( $E_{GW}$ ). At the low frequency end the coupling of fluctuations from the amplitude quadrature into the phase quadrature increases and the length of  $E_{RP}$  showing up in the phase quadrature becomes more and more dominant with lower frequency. While the GW signal stays constant in frequency, the change of  $E_{RP}$  significantly reduces the SNR of our measurement and therefore decreases the sensitivity towards the low frequency end of the measurement band. So, our picture allows us to explain the shape of the overall quantum noise spectrum (trace 1c). What will happen if we increase the optical power by a factor of 100? First of all the length of the GW arrow will increase by a factor of 10. At the same time the length of  $E_1$  and  $E_2$  stays constant, so that the overall signal-to-noise ratio at high frequencies increases by a factor of 10, i.e., the quantum noise contribution is reduced by a factor 10. However, since  $E_{RP}$  scales directly with the optical power, its length is now 100 times longer. So, at low frequencies the noise is increased by a factor of 100, whereas the length of the signal arrow  $E_{GW}$  is only increased by a factor of 10, so that in total we lose SNR at the low frequency end. Hence, our simple model predicts that for a factor 100 power increase we will obtain a factor 10 improvement with respect to the trace 1c at high frequencies and a factor 10 sensitivity reduction at low frequencies. These predictions match exactly the shape of the trace 2c in Fig. 11.3. So, our simple graphical tool has passed its first crucial test.

## 11.4 Squeezed Light Injection

In the previous section we already briefly discussed squeezed light and described it in the quadrature picture (see right-hand panel of Fig. 11.4). The squeezing ellipse can be characterized by three properties: (i) the squeezing level, i.e., ratio of diameter of the “unsqueezed” ball and the length of the minor axis of the “squeezed” ellipse, as well as the level of *anti-squeezing* which is given by the ratio of the ball diameter and the length of the major axis of the squeezing ellipse; (ii) the orientation of the squeezing ellipse in the quadrature plane, also referred to as *squeezing angle*; and (iii) the frequency of the squeezed light field. Squeezed states of light can in general be created by means of nonlinear optical effects, such as for instance an optic parametric oscillator (OPO). During the past decade there have been major advances in the generation of squeezed light for gravitational wave detectors such as the demonstration of squeezing levels of more than 12 dB [11] as well as squeezing down to frequencies of a few Hz [12]. Due to limited space in this chapter we will omit a detailed description of the generation of squeezed light states here. The interested

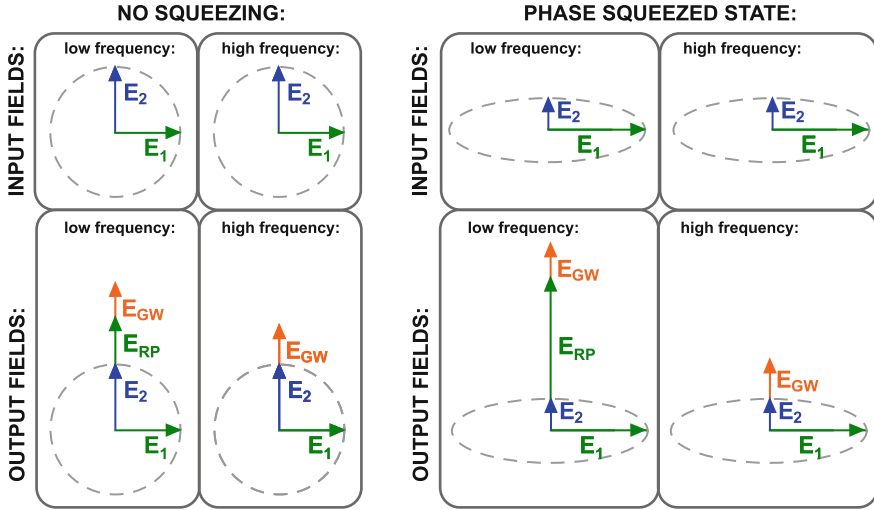


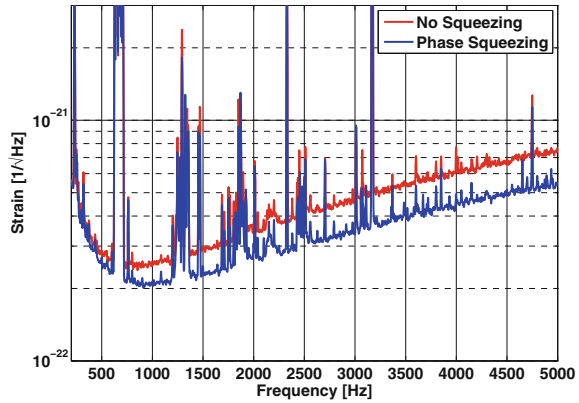
**Fig. 11.6** Quadrature picture for a simple Michelson interferometer with phase squeezing (*right*) and without squeezing (*left*) as reference

reader can find good overviews of the technical principles involved in the generation of squeezed light in [13, 14].

Let us now investigate how the application of squeezing can improve the sensitivity of a GW detector. Assuming we have produced sufficiently strong squeezing at the desired frequency, then the only other parameter we need to decide on is the orientation of the squeezing ellipse. If we want to increase the sensitivity of our GW detector at high frequencies then we should inject phase squeezing, i.e., the minor axis of the squeezing ellipse is oriented in parallel to the phase quadrature. Figure 11.6 illustrates the application of phase squeezing. The ball is squeezed so that  $E_2$  is shortened and  $E_1$  becomes longer. Since the magnitude of the GW signals stays constant, at high frequencies we can improve the signal-to-noise ratio and therefore improve the sensitivity of our interferometer. However, as indicated in the third panel of Fig. 11.6, at low frequencies the noise in the phase quadrature is strongly increased when applying phase squeezing, because the increased amplitude fluctuations originating from the anti-squeezing couple via radiation pressure into the phase quadrature ( $E_{RP}$ ). So, whereas the GW signal is independent of the squeezing level, the quantum noise at low frequencies increases with the application of phase squeezing and therefore overall we lose sensitivity at the low frequency end of the spectrum.

However, if we are keen to improve the interferometer sensitivity at low frequencies, this can also be accomplished by the injection of squeezed light. In this case we have to apply amplitude squeezing, so that the length of  $E_1$  is reduced and therefore also the radiation pressure noise coupling into the phase quadrature decreases. The consequence of this is improved low frequency sensitivity at the expense of reduced

**Fig. 11.7** Improvement of the GEO 600 sensitivity achieved by the injection of phase squeezing at the output port of the interferometer



sensitivity at high frequencies, because due to the anti-squeezing in that case  $E_2$  will be longer than in the unsqueezed case. Hence, we see that the application of purely phase-squeezed or purely amplitude-squeezed light only allows us to improve the sensitivity over a certain part of the detection band. From a qualitative point of view such squeezing in the ideal case (i.e., if the squeezing level is exactly the same as the anti-squeezing level) allows exactly the same sensitivity variations as is possible by increasing or decreasing the light power inside the interferometer.

It is not possible to surpass the SQL by application of purely phase-squeezed or purely amplitude-squeezed light.

GEO 600 was the first large-scale GW detector to routinely improve its sensitivity by the application of squeezed light [15]. The implemented squeezing source is able to produce phase squeezing of almost 10 dB, which would be equivalent to a factor 3 improvement in strain sensitivity. However, due to high optical losses (in particular in the output mode cleaner) the obtained sensitivity improvement is only about a factor  $\sqrt{2}$ . Please note that at low frequencies GEO 600 is limited by seismic and control noise, masking the expected increase of quantum noise at the low-frequency end which is a consequence of the injection of phase squeezed light.

The experience with long-term injection of squeezed light states at GEO 600 [16] together with the recent tests of squeezed light in the Hanford 2 km interferometer [17], transform squeezing from “science fiction” to an established tool for gravitational wave detection.

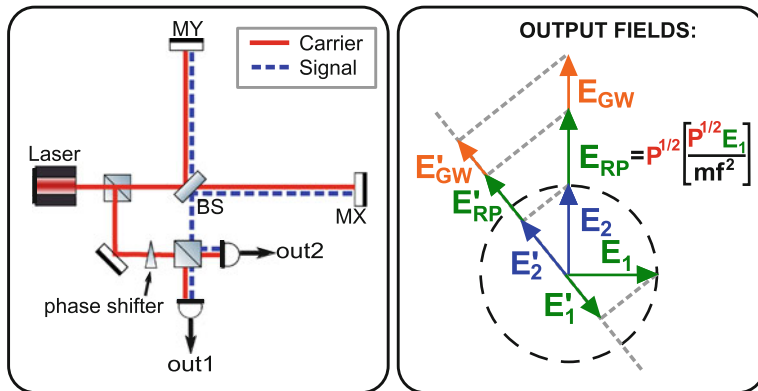


**Fig. 11.8** *Left panel* Schematic layout of a simple Michelson interferometer with homodyne readout. The output port is kept on destructive interference so that only the signal can leave towards the photodiodes, where it beats with light picked off before the interferometer. In order to avoid open ports a homodyne detector consisting of a pair of photodiodes is used. *Right panel* Illustration of radiation pressure noise cancellation via homodyne readout

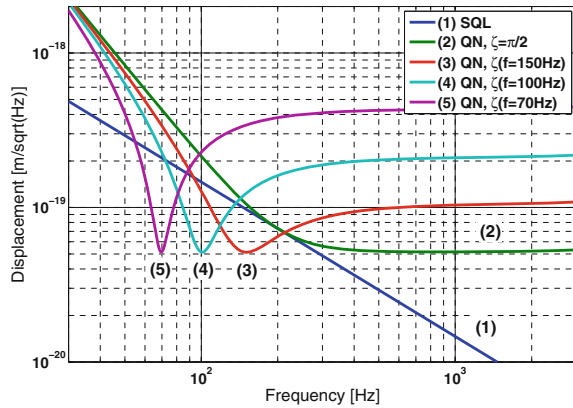
### 11.5 Homodyne Readout and Variational Readout

So far we have always assumed that we would read out our interferometer exactly in the phase quadrature. Naively thinking, this choice seems to make most sense because this gives us the strongest GW signal. However, as we will see in this section it can be beneficial to use a different readout angle, i.e., to readout a superposition of phase and amplitude quadrature.

From a technical point of view it is possible to vary this readout angle by utilizing a homodyne readout scheme as illustrated on the left-hand part of Fig. 11.8. Instead of using DC-readout [18, 19] in which a deliberate offset is introduced to make a fraction of the carrier field leak out through the output port forming the local oscillator for the gravitational wave signal. We can also pick off some light before the main interferometer and guide it to the output port where it can serve as local oscillator. The latter scheme is referred to as “homodyne readout.” By shifting the phase of the local oscillator with respect to the light leaving the main interferometer, for instance by microscopically changing the local oscillator path length, one can choose whether to read out the amplitude quadrature, the phase quadrature, or an arbitrary superposition of these.

So, how does the homodyne readout help us to reduce quantum noise? In order to understand this our graphical tool comes in handy again, as displayed on the right-hand panel of Fig. 11.8. Recall that the length of  $E_{RP}$  depends on the observation frequency. However, the length of  $E_1$ , which is correlated with  $E_{RP}$  and represents the noise in the amplitude quadrature is not frequency dependent. This means that for every frequency there is a specific readout angle for which the projections,  $E'_{RP}$  and  $E'_1$ , of the two correlated arrows ( $E_{RP}, E_1$ ) onto the readout axis have exactly

**Fig. 11.9** SQL and simulated quantum noise of the AEI 10 m sub-SQL interferometer for different readout angles. Using homodyne readout it is possible to exactly cancel radiation pressure noise at one frequency and to surpass the SQL in a narrow frequency range. The figure is taken from [20]



the same length. Since  $E'_{RP}$  and  $E'_1$  are correlated but point in opposite directions they exactly cancel out; thus our sensitivity is determined by the ratio of the lengths of the  $E'_{GW}$  and  $E'_2$ . In this case we have managed to cancel completely the radiation pressure noise at our measurement frequency. Please note that the ratio of the  $E'_{GW}$  and  $E'_2$  stays constant for any readout angle different from pure amplitude quadrature readout.

The experimental demonstration of radiation pressure noise cancellation via homodyne readout is one of the goals of the AEI 10 m sub-SQL interferometer [21, 22]. Figure 11.9 shows the simulated quantum noise for the AEI-10m interferometer for 4 different readout angles [20]. Trace 2 represents the standard case of pure phase quadrature readout. We see a flat shot noise spectrum at frequencies above a few 100 Hz (plus the additional roll-off at 10 kHz originating from the limited bandwidth of the arm cavity), and at low frequencies we see the characteristic increase in quantum noise due to radiation pressure noise, following a  $1/f^2$  characteristic. The other three traces show the quantum noise for a certain readout angle. As one can see it is possible to cancel the radiation pressure noise at one frequency and to dip down below the SQL achieving exactly the same peak displacement sensitivity as in the shot noise limited frequency regime of trace 2, i.e., the potential sensitivity improvement is limited by shot noise which was buried under quantum radiation pressure noise before.

A simple homodyne readout is one of the possibilities to achieve narrowband sub-SQL sensitivities.

Let us have a closer look at trace 4 in Fig. 11.9 and try to better understand its shape. We have already explained that we can completely cancel radiation pressure noise at one frequency, in this case 100 Hz. However, at frequencies below and above this “sweet spot” quantum noise is only partly reduced or even increased. Below 100 Hz

$E'_1$  is shorter than  $E'_{\text{RP}}$  and therefore the cancellation of the correlated noise terms works only partly. Finally we should explain why the noise represented by trace 4 is higher than the trace 2 for all frequencies above a few 100Hz where the trace 2 is made up of shot noise. At these high frequencies  $E'_{\text{RP}}$  is of negligible length. However, due to the rotated readout angle amplitude noise from  $E_1$  is mixed into our readout signal ( $E'_1$ ), so that the sensitivity is determined by the ratio of  $E'_{\text{GW}}$  and the sum of the uncorrelated noise contributions  $E'_2$  and  $E'_1$ .

So, we have seen that changing the readout quadrature (homodyne readout) allows us to cancel radiation pressure noise at a single frequency at the expense of reduced sensitivity at high frequencies. If it would be possible to change the readout angle in a frequency-dependent way, then it should be possible to cancel radiation pressure noise at low frequencies, i.e., where it dominates, without introducing additional noise at high frequencies. This technique, called *variational readout* can actually be realized by making use of the dispersion of the light reflected from a cavity [23], in analogy to the generation of frequency-dependent squeezing discussed in the following section.

## 11.6 Frequency-Dependent Squeezing

We have seen above that the injection of simple amplitude or phase squeezing cannot improve the sensitivity over the whole frequency range and therefore with such squeezed light states it is not possible to surpass the SQL. However, if we were to manage to change the squeezing angle of the injected light in a frequency-dependent way, then it should be possible to obtain a reduction of quantum noise at all frequencies, which in turn would allow broadband measurements with a sensitivity below the SQL.

Using our graphical tool, in Sect. 11.3.2 we learned that our sensitivity is limited at high frequencies by shot noise in the phase quadrature, while at low frequencies the dominant noise term originates from amplitude fluctuations coupled to the phase quadrature via radiation pressure-induced mirror motion. Hence, if we could rotate the squeezing ellipse as a function of the detection frequency to always provide squeezing in the optimal quadrature we could reduce quantum noise in the entire detection band.

Injection of squeezed light for which the squeezing angle is a function of frequency is in the following referred to as *frequency-dependent squeezing*.

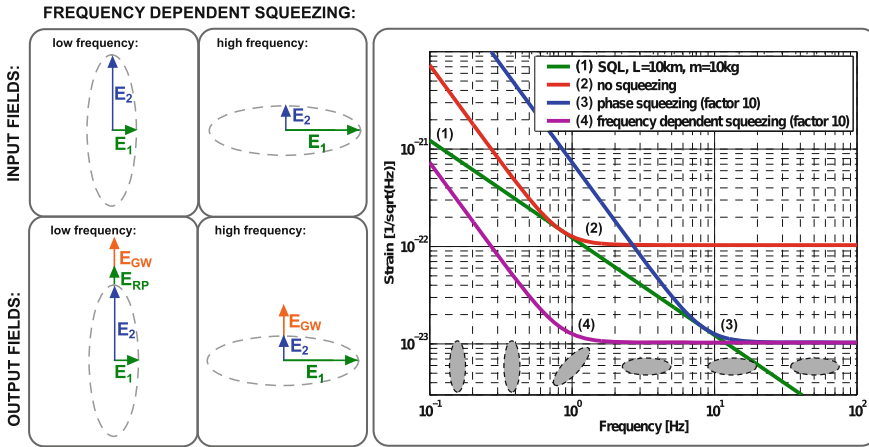


**Fig. 11.10** *Left* Illustration of frequency-dependent squeezing using the quadrature picture. *Right* Quantum noise of a simple Michelson interferometer with pure phase squeezing as well as frequency-dependent squeezing. Please note that even though theoretically a squeezing factor of 10 is possible, in real interferometers optical losses and control noise of the squeezing will degrade the sensitivity improvement. It is assumed that in future GW detectors quantum noise reduction by squeezing injection is limited to a factor of 3 to 4 [24]

The two left panels of Fig. 11.10 illustrate frequency-dependent squeezing in the quadrature picture. For all frequencies we readout the phase quadrature. At high frequencies we apply phase squeezing and obtain a quantum noise reduction exactly the same as for injection of frequency-independent phase squeezing. In contrast to this, towards the low frequency end of the detection band we arrange for the squeezing ellipse to continuously rotate from phase quadrature squeezing to squeezing in the amplitude quadrature. The key here is that the length of the original  $E_1$  arrow in the amplitude quadrature reduces, which results in less noise coupled to the phase quadrature via radiation pressure-induced mirror motion. Therefore, also the length of the  $E_{RP}$  arrow in the phase quadrature is reduced. As a consequence the SNR at low frequency is larger than in the unsqueezed case (compare to left panel of Fig. 11.6). The right-hand plot of Fig. 11.10 compares the quantum noise spectrum of a simple Michelson interferometer without squeezing (trace 2), pure phase squeezing (trace 3), and frequency-dependent squeezing (trace 4), where the gray ellipses at the bottom of the plot illustrate the optimized orientation of the squeezing ellipse of the injected squeezing at different frequencies in the detection band.

Frequency-dependent squeezing can provide a broadband reduction of quantum noise significantly below the SQL.

Frequency-dependent squeezing has been identified as one of the key technologies for the Einstein Telescope [25, 26] as well as for upgrades to the Advanced LIGO



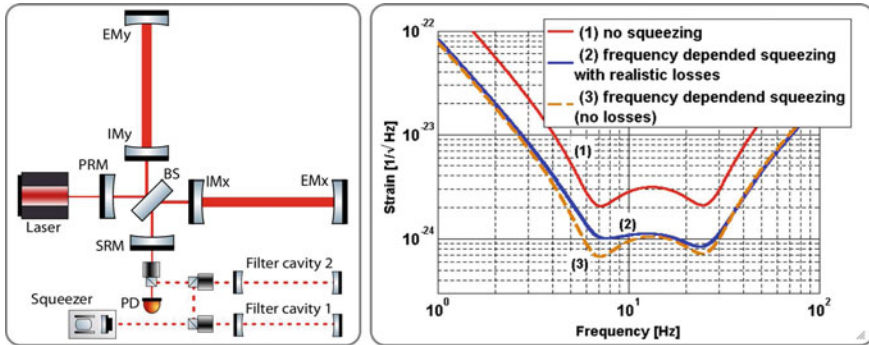


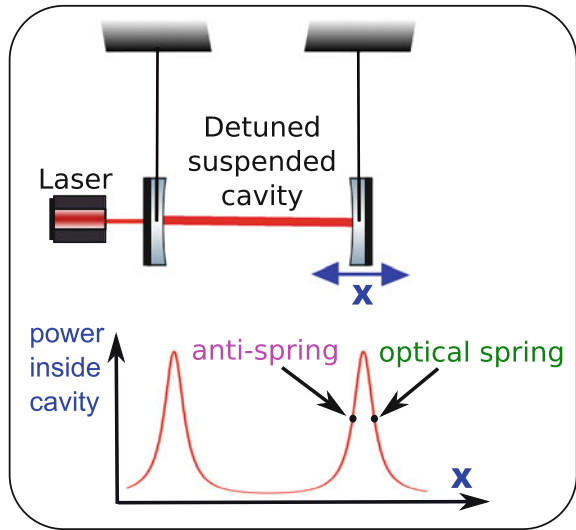
**Fig. 11.11** *Left* Cartoon of the optical layout of the ET low-frequency interferometer, which uses detuned signal recycling and exploits the dispersion of the squeezed light being reflected from two filter cavities to provide squeezing at the optimal frequency-dependent angle for all frequencies. *Right* Quantum noise for an ET low-frequency interferometer without squeezing (trace 1), with 6 dB of frequency-dependent squeezing injected into an ideal interferometer (trace 3) and frequency-dependent squeezing considering realistic losses (trace 2)

instruments [27, 28]. Figure 11.11 illustrates the implementation of frequency dependent squeezing into an ET low frequency interferometer. The squeezed light leaving the squeezing source is reflected from two slightly differently detuned cavities. The dispersion of the detuned cavities introduces the frequency dependent rotation of the squeezing ellipse. Afterwards the squeezed light is injected into the output port of the interferometer. For the squeezing injected into the detection port the interferometer acts as a reflector. The injected squeezing leaves the interferometer and co-propagates with the GW signal towards the detection stage where the squeezed output field is converted into an electronic signal.

From the technical point of view the key difficulties in realizing frequency-dependent squeezing are the design and low-noise operation of the filter cavities with the required bandwidth and low enough losses in order not to destroy the squeezing. In the case of the ET low-frequency interferometer the required bandwidth of the filter cavity is similar to the bandwidth of the signal recycling. As one can see from the right-hand plot of Fig. 11.11, for an ET low frequency interferometer the signal recycling bandwidth is about 10 Hz, which in turn requires to employ filter cavities of the same finesse and length as the main interferometer. If shorter filter cavities are preferred it is necessary to increase the finesse which, depending on the chosen length, may take on extremely high values.

In high-finesse filter cavities the presence of even very low optical losses may strongly degrade the squeezing strength of the generated frequency-dependent squeezing, as is illustrated in Fig 11.11. Whereas trace 3 shows the quantum noise level for filter cavities without any losses, trace 2 represents the quantum noise for 10 km long filter cavities with 75 ppm round-trip loss. Why are losses so important, even though we only use the filter cavities in reflection? The problem is that some of the squeezing (mainly at and around the resonances of the detuned filter cavities)

**Fig. 11.12** Illustration of the optical spring principle. In a cavity tuned slightly away from its resonance, the optical power strongly depends on the microscopic position of the mirrors or more accurately the cavity length. If one or both of the cavity mirrors are suspended, then they are susceptible to radiation pressure forces, which depend on the position of the mirror. Radiation pressure, together with gravity, acts as a linear restoring force, resembling the dynamics of a mechanical spring



actually enters the filter cavities and hence is subject to internal optical loss. Loss in this context means that a fraction of the squeezed field is lost and replaced by a coherent unsqueezed state. For constant optical loss per filter cavity mirror, the higher we choose the finesse of the filter cavity, the stronger is the squeezing degradation.

## 11.7 Optical Springs and Optomechanical Rigidity

An optical spring is a fascinating physical phenomenon, which allows to connect two or more suspended mirrors with springs completely made out of photons (also compare Chap. 12 of this book). These springs can be made kilometers long and stiffer than diamond [29, 30], while at the same time, in contrast to any mechanical spring, they are somewhat free from classical noise.

So how can we create an optical spring? The basic principle is shown in Fig. 11.12: in a detuned Fabry-Perot cavity featuring high optical power and at least one suspended mirror, the equilibrium position of the suspended mirror is given by radiation pressure trying to push the mirrors further apart and gravity pulling the suspended mirror to shorten the cavity. Now, let us consider the case labelled “optical spring” in Fig. 11.12 and let us try to push the right mirror away from equilibrium. In case we push the mirror to the right two things will change: first, gravity will try to pull the mirror back towards its equilibrium and secondly as the cavity length has increased the cavity power will decrease, as the cavity is pushed further away from resonance. Therefore, the radiation pressure force will decrease. Both these effects will cause the mirror to move towards the left back into its equilibrium position. Now let us try to push the mirror towards the left. As this means that we shorten the cavity and

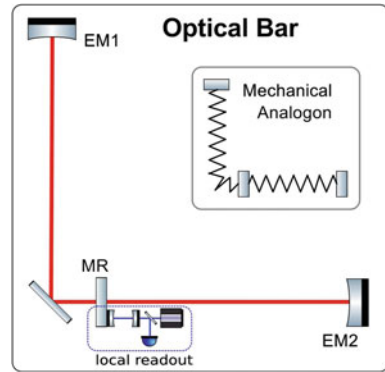
move closer to resonance, the cavity power increases and the increased radiation pressure force pushes the mirror back towards the equilibrium. So, we have a system exhibiting a linear restoring force, which can in simple terms be described by Hooke's law  $F = -kx$ , where  $F$  is the superposition of forces acting on the mirror,  $x$  is the distance of the mirror from its equilibrium point, and  $k$  is the effective spring constant.

In a cavity with two suspended mirrors connected by an optical spring, when we push one mirror (and keep it fixed so that it cannot return to its original position), then the other mirror will move exactly by the same amount, so that the pathlength for the light stays constant. Using this phenomenon one can control the position of a mirror over several kilometers of distance, just by acting on the second cavity mirror.

There are two more interesting aspects about optical springs worth to be mentioned here: When setting the cavity operation point onto the opposite slope of the Airy peak (labeled as “anti-spring” in Fig. 11.12), then it is easy to see that there will be an optical anti-spring, i.e., the radiation pressure force acts in the same direction as a mirror displacement. The other interesting aspect is related to the damping of optical springs: When changing the cavity length, the optical power does not settle immediately at its new value, but it takes some time for the light in the cavity to build up or relax. This kind of “delay” causes the optical spring to feature anti-damping. The anti-damping can render optical systems unstable if no counter measures are applied. Two ways have been proposed to avoid this problem: First of all one can use active feedback to introduce damping or one can use two different springs acting on the same system and combining them in a way such that the result is an effective spring with positive damping [31].

So, how can optical springs actually help to surpass the SQL? In this respect two concepts are of interest. First of all optical springs play an important role in the context of advanced GW detectors employing detuned signal recycling [32], which has already been discussed in detail in Chap. 3 of this book. The other class of concepts employs optical spring systems to act as transducer of the GW. Figure 11.13 shows the simplest variant of such a transducer configuration, a so-called *optical bar* [33]. Two detuned cavities with a heavy end mirror each (EM1 and EM2) share a lightweight mirror (MR) so that MR is connected via optical springs to both end test masses. In case a GW with a frequency below the optical spring frequency is incident on the detector perpendicular to the plane spanned by the interferometer arms, one of the arms will shrink, while the other will stretch. If you think about this in terms of a system of coupled mechanical springs, then this means that one spring will be squeezed, i.e., it will push on MR, while the spring in the perpendicular arm will be stretched and pull on MR, so that as a consequence in the presence of a GW the mirror denoted MR will move in its local frame. This local movement of MR can then be read out relative to a local reference. The trick of the optical bar topology is that this

**Fig. 11.13** Simplified optical layout of an optical bar. A lightweight mirror (MR) is connected via optical springs to two heavy end mirrors (EM1 and EM2). If there occurs a change in the differential armlength (e.g., due to GW), MR is displaced with respect to its local frame. A separate local readout can then be used to readout the GW signal



concept allows to separate the GW transducer from the readout process and hence gives the possibility to optimize both parts of the optical bar system independently to minimize quantum noise in the measurement. More advanced and more complex configurations involving optical springs, such as optical levers [34, 35] and local readout configurations [36] have been proposed in the literature, but due to lack of space will not be discussed here.

### 11.8 Speedmeter Topologies

We have seen above that Michelson interferometers are limited by the SQL. The reason for this is that quantum theory imposes a limitation on how accurate subsequent position measurements can be carried out. This is a direct consequence of the fact that position measurements at different times  $x(t)$ ,  $x(t')$  do not commute, i.e.,

$$[\hat{x}(t), \hat{x}(t')] \neq 0. \tag{11.9}$$

However, already in the 1930s John von Neumann realized that for some systems it is possible to find observables which are not limited by an uncertainty relation [37]. For instance in systems where the momentum is conserved you can in principle measure the momentum  $p$  of an ensemble of mirrors continuously with arbitrary precision since

$$[p(t), p(t')] = 0. \tag{11.10}$$

In 1990, Braginsky and Khalili proposed this concept for application in *bar detectors*, which were the predecessors of laser-interferometric GW detectors [38]. Hence,

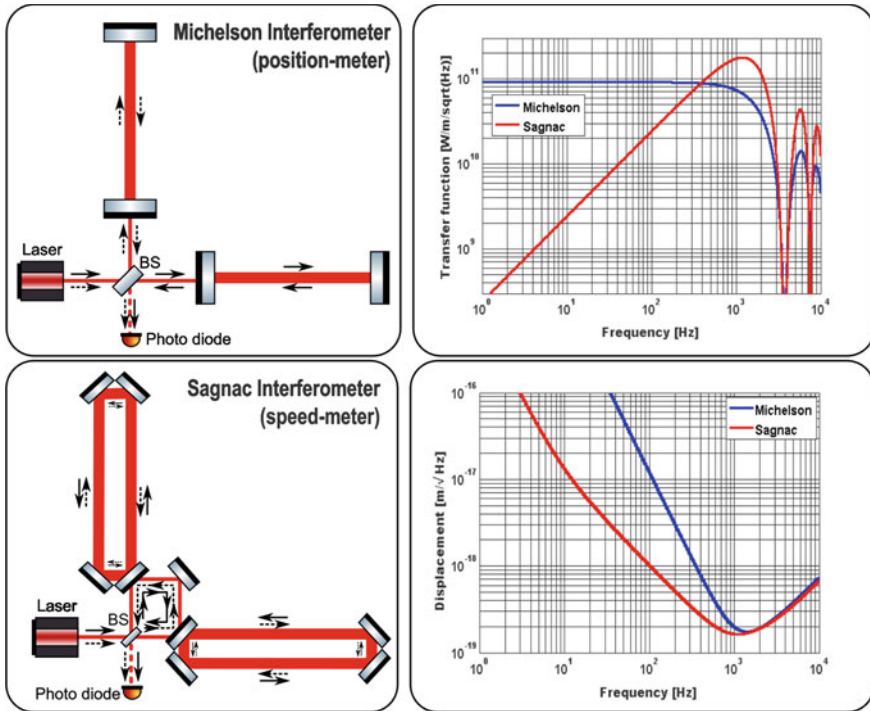


**Fig. 11.14** Simplified optical layout of a Michelson interferometer with arm cavities (*top left*) and a Sagnac interferometer with arm cavities (*bottom left*). Whereas in the case of the Michelson interferometer all photons only travel through one of the arms, in the case of the Sagnac interferometer all photons travel through both arms. Transfer functions from differential arm length to signal on the main photo detector (*top right*). Quantum noise limited effective “displacement” sensitivity for a Michelson and a Sagnac interferometer (*bottom right*)

for detectors of this type, in which the velocity would be measured instead of the position of the test mass, the name “speed-meter” was coined. Later, the concept was also suggested for application in interferometric GW detectors. The first speed-meter interferometer configuration was based on a Michelson interferometer with a so-called shloshing cavity at the output port the interferometer. With the aid of this shloshing cavity the conventional Michelson interferometer is transformed into a speedmeter [39]. In the year 2003, Chen demonstrated in a theoretical work that a Sagnac interferometer naturally constitutes a speedmeter [40].

In order to understand why a Sagnac interferometer is a natural representative of the class of speedmeters we should have a look at the optical layouts of a Michelson interferometer and a Sagnac interferometer as displayed in the two left-hand panels of Fig. 11.14. In a Michelson interferometer, depending on whether the photons in the input laser beam are transmitted or reflected, the light either travels along the horizontal or the vertical arm. It is important that when the returning photons

interfere at the beam splitter, each photon has only sensed the mirror positions of a single arm. Contrasting this, in a Sagnac interferometer all photons travel along both arm cavities, i.e., they sense the positions of all relevant mirrors. Only after all photons have passed through both arm cavities the light interferes again at the output port of the beam splitter. This means that the light initially transmitted through the beam splitter measures the position of the end mirrors of the horizontal arm at a time  $t_1$ , while it measures the position of the end mirrors in the vertical arm at a slightly later time  $t_2$ . The light initially reflected at the beam splitter measures the position of the end mirrors of the vertical arm at a time  $t_1$ , while it measures the position of the end mirrors in the horizontal arm at a slightly later time  $t_2$ . So, each of the end mirrors is sensed at two different times, or, in other words, we measure the velocity of the end mirrors, but not their absolute position.

As the Sagnac speedmeter is not sensitive to absolute displacement, its response to *absolute* differential arm lengths goes down to zero. This can be seen in the top right plot of Fig. 11.14. While the Michelson has a flat response at low frequencies, the Sagnac response falls linearly towards lower frequencies. So, if the signal at low frequencies is smaller in the Sagnac compared to the Michelson Interferometer, how can the quantum noise limited sensitivity be better for the speedmeter?

Please recall that the achievable sensitivity is related to the SNR. For the Michelson the signal is flat, but the radiation pressure noise is present and increases quadratically towards lower frequency. In contrast, in the Sagnac speedmeter the signal decreases linearly towards low frequency, while the noise is flat because the radiation pressure noise is mostly cancelled, resulting in a significantly reduced and constant value of the radiation pressure noise at low frequencies. So, in conclusion the Sagnac speedmeter wins in terms of low frequency sensitivity over the Michelson.

The slight bend in the Sagnac sensitivity trace below 10Hz (compare Fig. 11.14) originates from the presence of optical losses in the considered configuration.

## 11.9 Challenges Towards Sub-SQL Interferometry

It is a fabulous achievement that the advanced GW detectors such as Advanced LIGO are on the brink of reaching a sensitivity limited by the Heisenberg Uncertainty Limit for 40kg mirrors! However, further improvements are possible since the SQL does not really pose an *ultimate limit*. Above we have introduced, and briefly discussed, a wealth of concepts available to tackle the SQL and eventually surpass it.

It is important to point out that all of the discussed concepts are not exclusive in terms of their application, but many of them can be combined to maximize the sensitivity improvement. For instance, already at the moment GEO 600 uses phase

quadrature squeezing in combination with signal recycling. The baseline design for ET as well as upgrades to Advanced LIGO are likely to employ signal recycling with frequency-dependent squeezing, while at the same time speedmeters with squeezing and/or signal recycling have been proposed as alternatives to the well-established Michelson interferometers.

So far pure phase squeezing is the only example of a technique discussed in this chapter that has already been demonstrated in a km-scale GW detector. All other concepts have so far only been analyzed theoretically. Careful experimental verification of these techniques in table-top experiments and in suspended low-noise prototypes is urgently required to have these technologies available for installation in the future GW detectors, to outwit quantum mechanics and measure with sensitivities below the Standard Quantum Limit.

**Acknowledgments** The author acknowledges the support from the Science and Technology Facilities Council (STFC), UK, and the European Research Council (ERC-2012-StG: 307245). The author thanks Kenneth Strain, Stefan Danilishin, and Farid Khalili for many fruitful discussions. Christian Gräf and Neil Gordon have provided many useful comments on this manuscript. All interferometer sketches in this chapter have been drawn using Alexander Franzen's ComponentLibrary.

## References

1. V.B. Braginsky, F.Y. Khalili, *Quantum Measurement*, (Cambridge University Press, Cambridge, 1992)
2. S. Danilishin, F.Y. Khalili, Quantum measurement theory in gravitational-wave detectors. *Living Rev. Relativ.* **15**, 5 (2012). <http://www.livingreviews.org/lrr-2012-5>
3. H. Müller-Ebhard et al., Review of quantum non-demolition schemes for the Einstein Telescope, (2009) ET-note, <https://tds.ego-gw.it/itf/tds/file.php?callFile=ET-010-09.pdf>
4. H. Miao et al., Comparison of Quantum Noise in 3G Interferometer Configurations, (2012). <https://dcc.ligo.org/cgi-bin/private/DocDB/ShowDocument?docid=78229>
5. R. Abbott et al., AdvLIGO Interferometer Sensing and Control Conceptual Design, Technical note LIGO-T070247-01-I (2008)
6. GWINC website, <http://lhocds.ligo-wa.caltech.edu:8000/advligo/GWINC>
7. V.B. Braginsky, F.Y. Khalili, Quantum nondemolition measurements: the route from toys to tools. *Rev. Mod. Phys.* **68** (1996)
8. Y. Chen, Advanced interferometer configurations, in *Presentation at Australian-Italian Workshop on GW Detection*, Oct 2005, <https://dcc.ligo.org/LIGO-G050517-x0>
9. Y. Chen, Various ways to beat the standard quantum limit, in *Presentation at Aspen Workshop 2004*, <https://dcc.ligo.org/LIGO-G040210-x0>
10. C.M. Caves, Quantum-mechanical noise in an interferometer. *Phys. Rev. D* **23**, 1693–1708 (1981)
11. M. Mehmet et al., Squeezed light at 1550 nm with a quantum noise reduction of 12.3 dB. *Opt. Express* **19**(25), 25763 (2011)
12. H. Vahlbruch, S. Chelkowski, K. Danzmann, R. Schnabel, Quantum engineering of squeezed states for quantum communication and metrology. *N. J. Phys.* **9**(10), 371 (2007)
13. S. Chelkowski et al., Coherent control of broadband vacuum squeezing. *PRA* **75**, 043814 (2007)
14. K. McKenzie et al., Squeezing in the audio gravitational-wave detection band. *PRL* **93**, 161105 (2004)
15. J. Abadie et al., A gravitational wave observatory operating beyond the quantum shot-noise limit. *Nat. Phys.* **7**(12), (2011)



16. H. Grote et al., First long-term application of squeezed states of light in a gravitational-wave observatory. *PRL* **110**, 181101 (2013)
17. J. Abadie et al., Enhanced sensitivity of the LIGO gravitational wave detector by using squeezed states of light. Accepted for publication in *Nature Photonics*, (2013). doi:[10.1038/NPHOTON.2013.177](https://doi.org/10.1038/NPHOTON.2013.177)
18. R.L. Ward et al., DC readout experiment at the Caltech 40m prototype interferometer. *Class. Quantum Gravity* **25**, 114030 (2008)
19. S. Hild et al., DC-readout of a signal-recycled gravitational wave detector. *Class. Quantum Gravity* **26**, 055012 (2009)
20. C. Gräf, Optical design and numerical modeling of the AEI 10 m Prototype sub-SQL interferometer, Ph.D. thesis, University of Hannover, 2013
21. S. Gossler et al., The AEI 10 m prototype interferometer. *Class. Quantum Gravity* **27**(8), 084023 (2010)
22. C. Gräf, S. Hild, H. Lück, S. Gossler, B. Willke, K. Strain, K. Danzmann, Optical layout for a 10 m Fabry-Perot Michelson interferometer with tunable stability. *Class. Quantum Gravity* **29**( 7), 075003 (2012)
23. H.J. Kimble, Y. Levin, A.B. Matsko, K.S. Thorne, S.P. Vyatchanin, Conversion of conventional gravitational-wave interferometers into quantum nondemolition interferometers by modifying their input and/or output optics. *Phys. Rev. D* **65**, 022002 (2002)
24. S. Hild, Beyond the second generation of laser-interferometric gravitational wave observatories. *Class. Quantum Gravity* **29**(12) 124006 (2012)
25. M. Punturo et al., The third generation of gravitational wave observatories and their science reach. *Class. Quantum Gravity* **27**, 084007 (2010)
26. S. Hild et al., Sensitivity studies for third-generation gravitational wave observatories. *Class. Quantum Gravity* **28**(9), 094013 (2011)
27. B. Barr et al., LIGO 3 Strawman Design, Team Red, Technical Note LIGO-T1200046-v1 2012/01/30, <https://dcc.ligo.org/LIGO-T1200046-v1>
28. R. Adhikari, K. Arai, S. Ballmer, E. Gustafson, S. Hild, Report of the 3rd Generation LIGO Detector Strawman Workshop, Technical Note LIGO-T1200031-v3 2012/05/15, <https://dcc.ligo.org/LIGO-T1200031-v3>
29. T. Corbitt, D. Ottaway, E. Innerhofer, J. Pelc, N. Mavalvala, Measurement of radiation-pressure-induced optomechanical dynamics in a suspended Fabry-Perot cavity. *Phys. Rev. A* **74**, 021802 (2006)
30. T. Corbitt et al., An all-optical trap for a gram-scale mirror. *Phys. Rev. Lett.* **98**, 150802 (2007)
31. H. Rehbein et al., Double optical spring enhancement for gravitational-wave detectors. *Phys. Rev. D* **78**, 062003 (2008)
32. A. Buonanno, Y. Chen, N. Mavalvala, Quantum noise in laser-interferometer gravitational-wave detectors with a heterodyne readout scheme. *Phys Rev D* **67**, 122005 (2003)
33. V.B. Braginsky, F.Y. Khalili, Nonlinear meter for the gravitational wave antenna. *Phys. Lett. A* **218**, 167–174 (1996)
34. F.Y. Khalili, The optical lever intracavity readout scheme for gravitational-wave antennae. *Phys. Lett. A* **298**, 308–314 (2002)
35. S.L. Danilishin, F.Y. Khalili, Practical design of the optical lever intracavity topology of gravitational-wave detectors. *Phys. Rev. D* **73**, 022002 (2006)
36. H. Rehbein et al., Local readout enhancement for detuned signal-recycling interferometers. *Phys. Rev. D. Am. Phys. Soc.* **76**, 062002 (2007)
37. J. von Neumann, *Mathematische Grundlagen der Quantenmechanik* (Springer, Berlin, 1932)
38. B. Braginsky, F.Y. Khalili, Gravitational wave antenna with QND speed meter. *Phys. Lett. A* **147**, 251–256 (1990)
39. P. Purdue, Y. Chen, Practical speed meter designs for quantum nondemolition gravitational-wave interferometers. *Phys. Rev. D* **66**, 122004 (2002)
40. Y. Chen, Sagnac interferometer as a speed-meter-type, quantum-nondemolition gravitational-wave detector. *Phys. Rev. D* **67**, 122004 (2003)